JOURNAL OF AIRCRAFT
Vol. 32, No. 2, March–April 1995

Navier-Stokes Solutions for an Oscillating Double-Delta Wing

J. A. Ekaterinaris* and Lewis B. Schiff†
NASA Ames Research Center, Moffett Field, California 94035

Steady-state and unsteady Navier-Stokes solutions of the vortical flow over a double-delta wing configuration, consisting of a sharp leading-edge 76-deg sweep strake and a 40-deg sweep wing section are presented. The governing equations are solved numerically with an upwind-biased, implicit, iterative, and factorized numerical scheme. At fixed angles of incidence, the steady-state flow and the leeward-side vortex system resulting from the strake and wing vortices are investigated for subsonic, high Reynolds number flows. The unsteady flowfield development resulting from the large amplitude oscillatory motion of the wing around a mean angle of attack of $\alpha = 22.4$ deg, with an amplitude of 6.8 deg, is also investigated. Lag in the appearance of vortex breakdown caused by the pitch-up motion is found in accordance with the experiment. The computed unsteady solution is compared with available unsteady flow measurements at several phase angles during the oscillation cycle.

Introduction

INVESTIGATION of the vortical flowfield over delta wings at a high angle of attack is an active area of current theoretical and experimental research. The main feature of the flow over a delta wing at an angle of attack is the leeward-side vortex pattern resulting from the separation of the windward-side and leeward-side boundary layers from the wing leading edge. The energetic character of the leeward-side vortical flowfield provides nonlinear lift. This additional vortical lift has been successfully utilized in modern aircraft. As the angle of attack increases, the leeward-side leading-edge vortices are strengthened, and the lift of the delta wing increases until a critical angle of attack is reached where bursting of the vortices occurs. Downstream of the burst point reversed axial velocities are usually observed, and the breakdown is followed by a turbulent wake. Breakdown has adverse effects on the lift characteristics and may cause unsteady self-excited oscillatory motion. Understanding the mechanisms that generate vortex breakdown, and the ability to predict its occurrence, is crucial in efforts to improve current aircraft design and performance in flight at high angle of attack.

Due to its importance to the aerodynamic behavior of the delta wing, the phenomenon of vortex breakdown was studied extensively both by experimental and theoretical investigations. Most of the early experimental work on vortex breakdown was done for axisymmetric swirling flows confined in cylindrical tubes. For flows over delta wings, both bubble- and spiral-type vortex breakdowns were observed, depending on the angle of attack and the wing aspect ratio. The structure of the vortical flowfield and the effect of vortex breakdown over delta wings was the subject of several recent experimental investigations.[1–6] Various flow regimes, ranging from the low-speed regime to the transonic regime, were investigated. Different aspect ratio delta wings were examined, and bubble or spiral vortex breakdown was identified depending on the angle of attack and the aspect ratio. The flow over simple delta wings and double-delta wings was also studied recently by numerical solution of the Navier-Stokes equations.[7–10] The results of these numerical investigations were in good agreement with the experimental measurements, and both bubble- and spiral-type breakdown were identified.

Recent experimental work by Cunningham and den Boer[6] studied the vortical flowfield over a double-delta (strake-delta) wing configuration. Both flows at fixed angles of attack and the unsteady flow response resulting from forced oscillatory motion of the wing surface were investigated. The objectives of the present numerical study are first to validate and assess the accuracy of the present algorithm by comparison of the steady-state solutions with available experimental data and solutions obtained previously using a different numerical scheme. The grid resolution required for accurate simulations of the complex vortical flowfields at high incidences is also assessed. Finally, a detailed investigation of the leeward-side flowfield, both at various fixed angles of attack and for several angles of attack during the oscillation cycle, is performed. The steady-state and unsteady solutions at the same angle of attack are compared. Flow phenomena, including interaction of the strake and wing vortices as the angle of attack is increasing and vortex breakdown, are examined in the computed solutions. The unsteady numerical results are validated through comparison with available unsteady experimental measurements.

Computational Method

Governing Equations

The compressible formulation of the thin-layer Navier-Stokes equations was used to obtain the numerical solution. The strong conservation-law form of the governing equations for a curvilinear coordinate system (ξ, η, ζ) along the axial, circumferential, and normal direction, respectively, is as follows:

$$\partial_t \boldsymbol{Q} + \partial_\xi \boldsymbol{E} + \partial_\eta \boldsymbol{F} + \partial_\zeta \boldsymbol{G} = Re^{-1} \partial_\zeta \boldsymbol{S} \tag{1}$$

here, $\boldsymbol{Q}$ is the dependent variable vector; $\boldsymbol{F}$, $\boldsymbol{G}$, $\boldsymbol{H}$ are the inviscid flux vectors; and $\boldsymbol{S}$ is the viscous term in the normal direction. These terms are given by

$$\boldsymbol{Q} = \frac{1}{J}\begin{bmatrix} \rho \\ \rho u \\ \rho v \\ \rho w \\ e \end{bmatrix}, \qquad \boldsymbol{E} = \frac{1}{J}\begin{bmatrix} \rho U \\ \rho u U + \xi_x p \\ \rho v U + \xi_y p \\ \rho w U + \xi_z p \\ (e + p)U - \xi_t p \end{bmatrix}$$

Presented as Paper 91-1624 at the AIAA 22nd Fluid Dynamics, Plasma Dynamics, and Lasers Conference, Honolulu, HI, June 24–26, 1991; received April 22, 1993; revision received June 2, 1994; accepted for publication June 14, 1994.

*Research Associate Professor, Navy—NASA Joint Institute of Aeronautics, Naval Postgraduate School, Department of Aeronautics and Astronautics. Senior Member AIAA.

†Special Assistant for High Alpha Technology, Fluid Dynamics Division. Associate Fellow AIAA.

$$\boldsymbol{F} = \frac{1}{J}\begin{bmatrix} \rho V \\ \rho u V + \eta_x p \\ \rho v V + \eta_y p \\ \rho w V + \eta_z p \\ (e + p)V - \eta_t p \end{bmatrix}, \qquad \boldsymbol{G} = \frac{1}{J}\begin{bmatrix} \rho W \\ \rho u W + \zeta_x p \\ \rho v W + \zeta_y p \\ \rho w W + \zeta_z p \\ (e + p)W - \zeta_t p \end{bmatrix}$$

$$\boldsymbol{S} = \frac{1}{J}\begin{bmatrix} 0 \\ \mu m_1 u_\zeta + (\mu/3) m_2 \zeta_x \\ \mu m_1 v_\zeta + (\mu/3) m_2 \zeta_y \\ \mu m_1 w_\zeta + (\mu/3) m_2 \zeta_z \\ \mu m_1 m_3 + (\mu/3) m_2 m_4 \end{bmatrix}$$

Here

$$m_1 = \zeta_x^2 + \zeta_y^2 + \zeta_z^2$$

$$m_2 = \zeta_x u_\zeta + \zeta_y v_\zeta + \zeta_z w_\zeta$$

$$m_3 = \left(\frac{1}{2}\right)\frac{\partial}{\partial \zeta}(u^2 + v^2 + w^2) + \frac{1}{Pr(\gamma - 1)}\left(\frac{\partial a^2}{\partial \zeta}\right)$$

$$m_4 = \zeta_x u + \zeta_y v + \zeta_z w$$

a is the local speed of sound, and U, V, and W are the contravariant velocity components given by $U = u\xi_x + v\xi_y + w\xi_z + \xi_t$, etc. In the above equations all geometrical dimensions are normalized with the wing-root chord length; ρ is the density normalized with respect to the freestream density ρ_∞; u, v, and w are the Cartesian velocity components normalized with the freestream speed of sound a_∞; e is the total energy per unit volume normalized with $\rho_\infty a_\infty^2$; and Pr is the Prandtl number. The pressure is related to the density and total energy through the equation of state for an ideal gas, $p = (\gamma - 1)[e - \rho(u^2 + v^2 + w^2)/2]$.

Numerical Implementation

The numerical integration of the governing equations is performed using a factorized, upwind-biased, iterative, implicit numerical scheme. This numerical procedure,[11,12] has been used with success for the computation of unsteady three-dimensional flows.[13] Implicit time integration is performed with the following factorized iterative numerical scheme:

$$\begin{aligned}
&[I + h_\xi(\nabla_\xi \tilde{A}^+_{i,j,k} + \Delta_\xi \tilde{A}^-_{i,j,k})]^p \times [I + h_\eta(\nabla_\eta \tilde{B}^+_{i,j,k} \\
&\quad + \Delta_\eta \tilde{B}^-_{i,j,k})]^p \times [I + h_\zeta(\nabla_\zeta \tilde{C}^+_{i,j,k} + \Delta_\zeta \tilde{C}^-_{i,j,k} \\
&\quad - Re^{-1}\delta_\zeta \tilde{M}_{i,j,k})]^p \times (\tilde{Q}^{p+1}_{i,j,k} - \tilde{Q}^p_{i,j,k}) \\
&\quad = -[\tilde{Q}^p_{i,j,k} - Q^n_{i,j,k} + h_\xi(\hat{E}^p_{i+1/2,j,k} - \hat{E}^p_{i-1/2,j,k}) \\
&\quad + h_\eta(\hat{F}^p_{i,j+1/2,k} - \hat{F}^p_{i,j-1/2,k}) + h_\zeta(\hat{G}^p_{i,j,k+1/2} \\
&\quad - \hat{G}^p_{i,j,k-1/2}) - Re^{-1}h_\zeta(\hat{S}^p_{i,j,k+1/2} - \hat{S}^p_{i,j,k-1/2})]
\end{aligned} \tag{2}$$

Here, $h_\xi = \Delta\tau/\Delta\xi$, $h_\eta = \Delta\tau/\Delta\eta$, and $h_\zeta = \Delta\tau/\Delta\zeta$. $\tilde{A}^\pm = (\partial\hat{E}/\partial\tilde{Q})$, $\tilde{B}^\pm = (\partial\hat{F}/\partial\tilde{Q})$, and $\tilde{C}^\pm = (\partial\hat{G}/\partial\tilde{Q})$ are the flux Jacobian matrices, and $\tilde{M}$ is the viscous flux Jacobian. The quantities $\hat{E}_{i+1/2,j,k}$, $\hat{F}_{i,j+1/2,k}$, $\hat{G}_{i,j,k+1/2}$, and $\hat{S}_{i,j,k+1/2}$ are numerical fluxes.

Time accuracy of the numerical solution is obtained by performing subiterations to convergence within each time step. The approximation to $\tilde{Q}^{n+1}$ at each subiteration is the quantity $\tilde{Q}^p$. During a given level of subiteration to convergence $\tilde{Q}^p \to Q^{n+1}$, when $p = 1$ and no subiterations are performed, then $\tilde{Q}^p = \tilde{Q}^n$ and $\tilde{Q}^{p+1} = \tilde{Q}^{n+1}$. Different upwinding schemes may be used to evaluate the fluxes $\hat{E}_{i+1/2,j,k}$, $\hat{F}_{i+1/2,j,k}$, and $\hat{G}_{i+1/2,j,k}$. Linearization and factorization errors can be eliminated during the iteration process, because the left side of Eq. (2) can be driven to zero at each time step. A vertex-based scheme is used, and the numerical fluxes along each direction are computed in the middle of the corresponding vertices. A third-order-accurate upwind-biased scheme is used to evaluate the fluxes. The flux $\hat{E}$, e.g., is evaluated as follows:

$$\begin{aligned}
\hat{E}_{i+1/2,j,k} &= \tfrac{1}{2}[\tilde{E}(Q_{i,j,k}) + \tilde{E}(Q_{i+1,j,k})] \\
&\quad + \tfrac{1}{6}[\Delta E^+(Q_{i-1,j,k}, Q_{i,j,k}) - \Delta E^+(Q_{i,j,k}, Q_{i+1,j,k})] \\
&\quad + \tfrac{1}{6}[\Delta E^-(Q_{i,j,k}, Q_{i+1,j,k}) - \Delta E^-(Q_{i+1,j,k}, Q_{i+2,j,k})]
\end{aligned} \tag{3}$$

the other fluxes, $\hat{F}$ and $\hat{G}$, are obtained in a similar manner.

The flux differences in Eq. (3) may be computed with different schemes. In the present code the flux differences $\Delta E^\pm$ are evaluated by Roe's scheme as $\Delta E^+(Q_{i,j,k}, Q_{i+1,j,k}) = \tilde{A}^\pm(Q_{i+1/2,j,k}) \times (Q_{i+1,j,k} - Q_{i,j,k}) = \tilde{A}^\pm(\bar{Q}) \times (Q_R - Q_L)$. Roe's approximate Riemann solver makes a linear wave decomposition and uses an average state $\bar{Q}$ defined as a function of the left and right states Q_L and Q_R to evaluate $E^\pm$. Roe-type flux-difference splitting requires explicit evaluation of the intermediate state $\bar{Q}$ for the construction of the flux-difference quantities. The intermediate state $\bar{Q}$ is calculated using the Roe variables $\bar{\rho} = \sqrt{\rho_L} + \sqrt{\rho_R}$, $\bar{u} = (u_L\sqrt{\rho_L} + u_R\sqrt{\rho_R})/\bar{\rho}$, etc. Linearization of the flux with Roe's scheme[14] requires a large computing effort. Therefore, linearization was performed as in Ref. 11 using the Steger-Warming[15] flux vector splitting, and the resulting linearization error was removed by subiterating to convergence at each time step. Typically, two to three Newton iterations were sufficient to drop the residuals two orders of magnitude. The viscous fluxes $\hat{S}_{i,j,k+1/2}$ are computed using central differences.

The experimental Reynolds number based on the root chord is $Re_c = 4.0 \times 10^6$, therefore, it is expected that the flow is turbulent over most of the wing surface. Transitional flow is expected to have an effect in regions very close to the leading edge. Present knowledge about transition does not enable computation and modeling of the transitional regime. Therefore, in the computations, the flow was considered to be fully turbulent. The Baldwin-Lomax eddy viscosity model,[16] as modified by Degani and Schiff[17] for the computation of separated vortical flows, was used throughout.

The strake delta wing configuration used for the numerical simulation is the same as the one used for the measurements of Ref. 6. It consists of a sharp leading-edge, 76-deg sweep strake having a diamond cross section, connected to a 40-deg sweep wing section formed by NACA 64A005 sections. All the dimensions of the experimental model are well-defined and the surface geometry can be defined algebraically. The surface grid and the dimensions of the wing normalized by the root chord are shown in Fig. 1a. Most of the solutions are obtained on a baseline $82 \times 63 \times 64$ point spherical grid. A sample spherical grid configuration employed for the computations of the double-delta wing is shown in Fig. 1b. The grid boundaries were placed 2–2.5 root chord lengths away from the wing surface, and sufficient clustering was used in the normal direction to enable capturing of the surface viscous layers. The steady-state solution of the $\alpha = 19$-deg angle-of-attack case is computed using a $82 \times 117 \times 64$ point grid having increased resolution in the circumferential direction.

For the unsteady solutions, a $92 \times 88 \times 71$ point grid is used. This grid has increased resolution in the leeward side where 56 out of the 88 circumferential points are located. On the windward side the resolution is similar to the baseline grid. The oscillatory motion of the wing is obtained by moving the grid. At the subsonic inflow boundary the density, normal and circumferential velocities, and the pressure are specified using characteristic variables, while the axial velocity is evaluated explicitly using zero-order Riemann invariant extrapolation. For the subsonic outflow boundary the pressure is specified, the streamwise velocity is evaluated using zero-order Riemann invariant extrapolation, while the density and the other two velocity components are extrapolated from the interior using first-order extrapolation. The fluid velocity on the solid surface is set equal to the prescribed velocity of the body for the unsteady solution, and zero for the steady-state solutions.

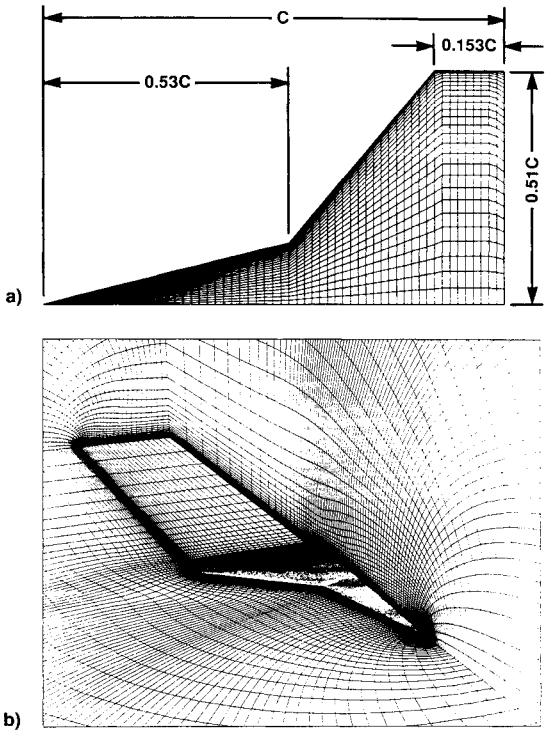

Fig. 1 Surface geometry and spherical grid over the double delta wing.

Results and Discussion

The experimental conditions of Ref. 6 were used for the numerical simulations. The freestream Mach number was $M_\infty = 0.22$, and the Reynolds number based on the root chord length was $Re_c = 4.0 \times 10^6$. Solutions were obtained for fixed angles of attack $\alpha = 10$, 19, and 22.4 deg. All solutions were computed as fully turbulent using the Baldwin-Lomax eddy viscosity model[16] as modified by Degani and Schiff.[17] For the lower angle-of-attack case, $\alpha = 10$ deg, the strake and wing vortices did not merge and no vortex breakdown was developed. At higher angles of attack ($\alpha = 19$ and 22.4 deg), the computed flows, as well as the flow visualization studies of Ref. 6, showed vortex merging and development of vortex breakdown. At $\alpha = 19$ deg the two vortices merged and vortex breakdown was found. The flow at $\alpha = 22.4$ deg also showed vortex merging and breakdown further upstream above the wing surface. In the following sections the steady-state flow regimes where the vortices remain distinct and the flow regime where the two vortices merge are presented first.

The unsteady solution for the oscillatory motion with $\alpha(t) = [22.4 + 6.8 \sin(\omega t)]$ deg with a reduced frequency of $k = \omega c/2U_\infty = 0.24$ was obtained. The unsteadiness was introduced through rigid body rotation of the grid around an axis at $x/c = 0.75$. The space matrices ξ_x, ξ_y, etc., were recalculated each time step to account for the new grid orientation, and the unsteady metrics ξ_t, η_t, and ζ_t were evaluated from the instantaneous rotation speed $\dot{\alpha} = d\alpha(t)/dt$ of the prescribed rigid body motion. The unsteady solutions at the peak of the cycle, and at the mean angle during the pitch-down and pitch-up motion are compared with available experimental data. The unsteady solution during pitch-up and pitch-down through $\alpha = 22.4$ deg is also compared with the corresponding fixed angle-of-attack solution in order to demonstrate the effect of the unsteady motion on the leeward-side vortical flowfield and vortex breakdown development.

Steady-State Solutions

Flowfields at fixed angles of attack were previously computed[18] using a partially upwind second-order accurate numerical scheme. In Ref. 18, upwinding along the streamwise

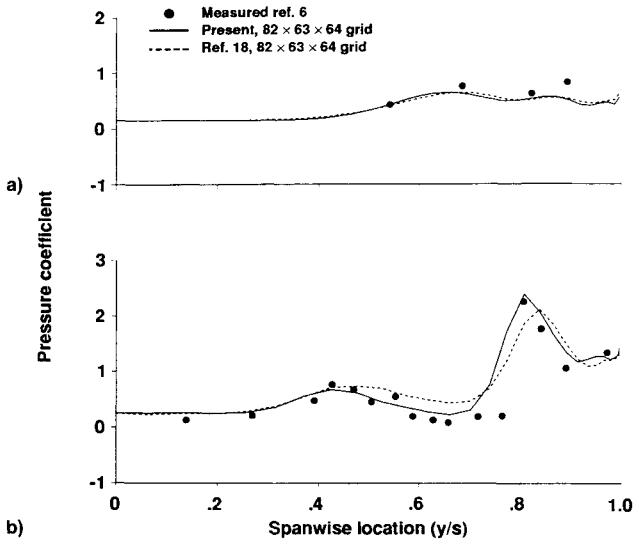

Fig. 2 Comparison of the leeward-side surface pressure coefficient at x/c = a) 0.4 and b) 0.65; $M_\infty = 0.22$, $\alpha = 10.0$ deg, $Re_c = 4.0 \times 10^6$ (turbulent).

direction was obtained by the Steger-Warming[15] flux-vector splitting, and central differencing was used in the other two directions. An upwind-biased numerical scheme presented previously, with inviscid fluxes evaluated by Roe's method and third-order accuracy, was used here. It was found that the upwind-biased scheme can provide solutions having the same accuracy on sparser grids than the ones obtained using the numerical scheme of Ref. 18. Grid resolution studies, where the circumferential resolution was increased, have shown that higher grid resolution is required for the second-order central differencing scheme to achieve the same solution quality. In order to validate the numerical procedure, comparisons between the solutions obtained with both schemes will be shown in the following sections. The fully upwind-biased scheme used here requires larger computing time per time step when subiterations are used. It was utilized, however, because of its robustness and the accuracy it provides.

Flow at $\alpha = 10.0$ Deg

The solution at $\alpha = 10$ deg was computed on the baseline, spherical, 82 × 63 × 64 point grid. The computed and measured surface pressure coefficient[6] on the strake section ($x/c = 0.4$) and the wing section ($x/c = 0.65$) are compared in Figs. 2a and 2b, respectively. The surface pressure coefficient obtained from the solution using the axially upwind scheme of Ref. 18 is shown for comparison with a dashed line. The weak suction peak caused by the primary vortex on the strake section is captured reasonably well by both numerical solutions. On the wing section the strength and the location of the suction peak caused by the strake vortex that convects over the wing is also predicted closely by both solutions. The strength of the suction peak caused by the wing vortex is predicted closely, and its location is found to be in agreement with the experiment.[6] The numerical solution with the present scheme predicted a slightly better surface pressure distribution for the wing compared to the solution of Ref. 18. It is believed that the grid resolution used for the computation of the flow at $\alpha = 10$ deg is sufficient, and a grid refinement study was not performed for this angle of attack. At this angle of incidence the two vortices remain distinct and little interaction can be observed at the strake-wing junction. The strake vortex follows a straight path at an angle to the leading edge over the strake section, and the flow is approximately conical. The leeward-side flow structure obtained with the present solution is very similar to the one obtained with the solution of Ref. 18.

Flow at α = 19.0 Deg

The solution at α = 19 deg was computed on the baseline, spherical, 82 × 63 × 64 point grid. A solution with a circumferentially refined 82 × 117 × 64 point grid was also computed. The computed surface pressure coefficients with the baseline and the circumferentially refined grids at x/c = 0.4 and x/c = 0.65 are compared with the measurements[6] in Figs. 3a and 3b, respectively. The suction peak caused by the primary vortex on the strake section is slightly underpredicted by the numerical solution. On the wing section the location of the suction peak caused by the strake vortex that convects over the wing, and the primary wing vortex is predicted closely. The strength of the strake vortex suction peaks are underpredicted by both the baseline and the refined grid solution. Grid refinement in the circumferential direction yielded better predictions only for the wing vortex suction peak.

The computed surface pressure coefficients at x/c = 0.65, using the present upwind-biased scheme and the partially upwind scheme of Ref. 18, for both the baseline grid and the circumferentially refined grid, are compared in Fig. 4. The strake vortex suction peak was underpredicted using both schemes, and grid refinement in the circumferential direction yielded little improvement. The predictions of the wing vortex

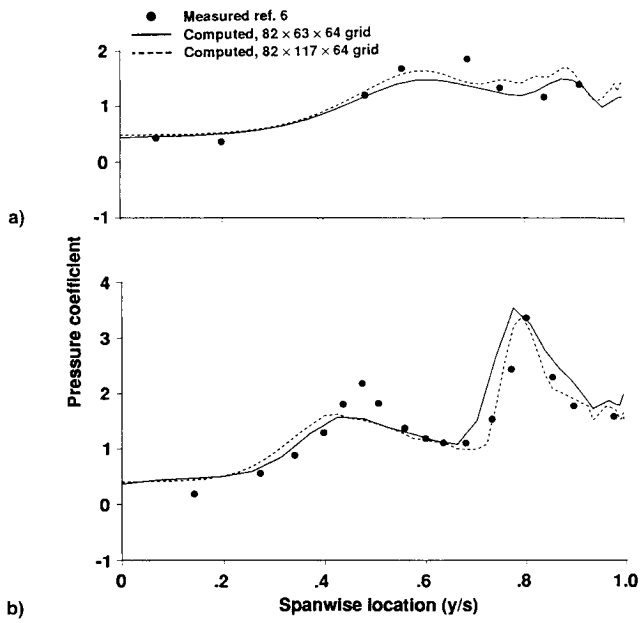

Fig. 3 Comparison of the leeward-side surface pressure coefficient at x/c = a) 0.4 and b) 0.65; M_∞ = 0.22, α = 19.0 deg, Re_c = 4.0 × 10^6 (turbulent).

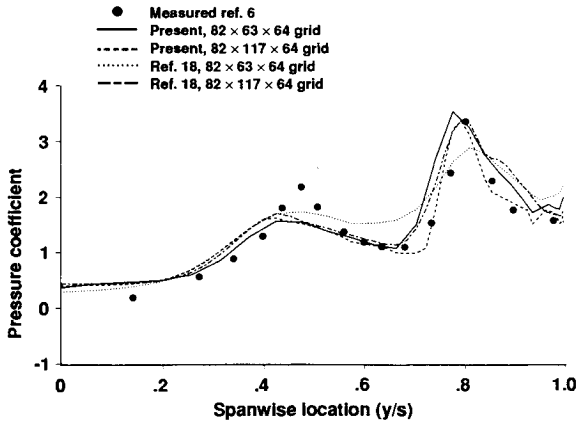

Fig. 4 Effect of grid resolution and numerical algorithm on the computed leeward-side surface pressure coefficient; x/c = 0.65, M_∞ = 0.22, α = 19.0 deg, Re_c = 4.0 × 10^6 (turbulent).

suction peak using the partially upwind scheme and the circumferentially refined grid matched the predictions of the present scheme with the baseline grid. This indicates that the higher-order-accuracy, upwind-biased scheme gives equivalent results using smaller grid densities. Therefore, the present numerical scheme was utilized for the simulation of unsteady flows.

The computed leeward-side flow structure showed that the strake and wing vortices remain distinct over most of the wing, and stronger interaction can be observed compared to the computed flow at 10-deg angle of attack. At the trailing-edge region, the two vortices merge and the wing vortex suffers breakdown. The strake vortex follows an *S*-shape path. Interaction with the wing vortex causes deflection of the strake vortex path towards the wing surface, and after merging the strake vortex is swept beneath the wing vortex. The leeward-side flow structure computed with the present solution is also in agreement with the numerical predictions of Ref. 18.

Flow at α = 22.4 Deg

The solution at α = 22.4 deg was computed on the baseline spherical, 82 × 63 × 64 point grid. The computed and measured[6] surface pressure coefficients at x/c = 0.4 and x/c = 0.65 are compared in Figs. 5a and 5b, respectively. The predictions of the surface pressure coefficient from the solutions of Ref. 18 with the baseline and the circumferentially refined grids are also shown. The suction peak caused by the primary vortex on the strake section is slightly underpredicted by the numerical solution. On the wing section the location of the suction peaks caused by the strake vortex that convects over the wing and the primary wing vortex are predicted closely. The strength of the strake vortex suction peak is again underpredicted by the present numerical solution. Lack of sufficient grid resolution is evident for the solution obtained with the axially flux-split scheme,[18] where the strength of both suction peaks is underpredicted, and the correct pressure distribution between the two vortices is not obtained. The solution obtained with the refined grid yielded better predictions, however, even higher resolution is required. For this case a solution using the present scheme and a grid refined in the circumferential direction was not obtained.

At this angle of incidence the two vortices remain distinct over a smaller part of the wing surface compared to the 19-

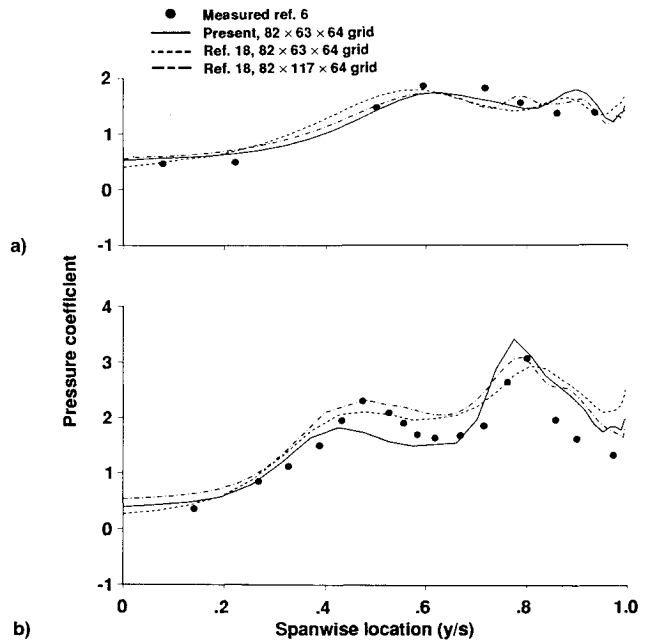

Fig. 5 Comparison of the leeward-side surface pressure coefficient at x/c = a) 0.4 and b) 0.65; M_∞ = 0.22, α = 22.4 deg, Re_c = 4.0 × 10^6 (turbulent).

deg angle-of-attack case. Over the wing and close to the trailing-edge region the two vortices merge and the wing vortex suffers breakdown. The breakdown region has a larger extent compared to the lower angle-of-attack case, however, significant flow unsteadiness is not observed in the computations.

Unsteady Flow Solutions

The steady-state solutions show that the baseline grid provides sufficient resolution to capture the flow physics at low angles of attack. At higher angles of attack, grids with additional resolution would be required for accurate computation of the complex leeward-side flow characteristics. One region where finer grid resolution is needed is in the vicinity of the strake vortex. In the previous section it was shown that the relative location of the strake vortex changes with the angle of attack, and covers a relatively large region of the leeward side. Solutions with grids that are locally refined in the vortical flow region[19,20] showed that significant improvements of the predictions of the vortical flowfield may be obtained. High grid densities in the vortex core region yield the proper strength of the leading-edge vortices, which otherwise diffuse in the coarser grids usually applied away from the body surface. The validity of the local grid refinement approach was investigated for steady-state flows,[19,20] but its application to unsteady flows is not straightforward because of the interpolation errors at the grid interfaces. In addition, it is not usually possible to estimate a priori the region where grid refinement is needed for an unsteady solution. Since the solution with the circumferentially refined grid showed some improvement, a single block, refined 92 × 88 × 71 point grid is used for the unsteady solution.

Plunging Motion

The ability of the numerical scheme to compute the unsteady flow response, and the accuracy of the unsteady solutions was first verified. It is well known that the steady flow over a wing at an angle of attack α and freestream speed U_∞ is equivalent to the flow with the wing in plunging motion at zero angle of attack, constant vertical speed $u_p = U_\infty \sin(\alpha)$, and horizontal or freestream speed of $U_\infty \cos(\alpha)$. The three-dimensional flowfield resulting from plunging motion of the double-delta wing, equivalent to a steady flow at $\alpha = 10$ deg, was computed on the baseline grid. The converged solution compared well with the experimental data and the steady-state solution. Comparison of the surface pressure coefficient distribution (not shown) indicated very good agreement with the corresponding fixed angle-of-attack steady-state solution.

Oscillatory Motion

The unsteady flow response resulting from the oscillation of the double-delta wing about a horizontal axis located at $x/c = 0.75$ is computed. The angle of attack varies as $\alpha(t) = [22.4 + 6.8 \sin(\omega t)]$ deg. The reduced frequency of the oscillation is $k = \omega c/2U_\infty = 0.24$, and $M_\infty = 0.22$. The oscillation of the experiment[6] was at a frequency $f = 8$ Hz. The experimental investigation showed that for this motion the vortices during the pitch-up initially do not suffer vortex breakdown, and that vortex breakdown develops at higher angles of attack compared to the static case. The unsteady solution starts from a converged steady-state solution for the flowfield at the minimum angle of attack $\alpha = 15.6$ deg during the cycle, and 2.5 cycles of oscillation are completed. Two subiterations are performed and 20,000 time steps are used for the computation of a full cycle. This number of time steps per cycle corresponds to a nondimensional time step $\Delta t = 0.003$, or a maximum Courant number $Cu \approx 600$.

The computed normal force during the oscillation cycle is compared in Fig. 6 with experimental values. Loads computed during the second cycle are used for this comparison. The computed normal force during the first half of the third cycle is identical to the one shown in Fig. 6. The computed normal force hysteresis loop is in good agreement with the experiment during the pitch-up part of the cycle. Small deviations from the experiment are obtained at the peak of the cycle and for the pitch-down motion, but the experimental trends are reproduced well.

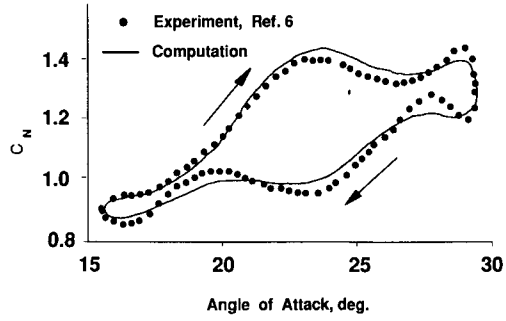

Fig. 6 Computed normal force coefficient; $M_\infty = 0.22$, $\alpha(t) = [22.4 + 6.8 \sin(\omega t)]$ deg, $k = 0.24$, $Re_c = 4.0 \times 10^6$ (turbulent).

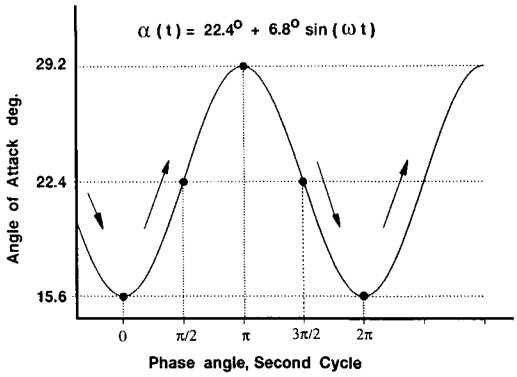

Fig. 7 Schematic of the oscillation cycle.

Further comparisons of the unsteady solutions with the experiment are presented at the angles of attack and phase angles shown schematically in Fig. 7. The computed surface pressure coefficients at $x/c = 0.65$ for different phase angles of the oscillation cycle are compared with the measurements in Figs. 8a–8d. The surface pressures comparison at the lower angle of the oscillation cycle, phase angle $\phi = 0.0$ or $\phi = 2\pi$, is shown in Fig. 8a. Time periodic response has been reached and the predictions at both phase angles are identical. The surface pressure coefficient at the mean angle-of-attack $\alpha = 22.4$ deg and phase angle $\phi = \pi/2$ is compared with the steady and unsteady data in Fig. 8b. For this phase angle the pitch rate is a positive, pitch-up case, and the computed unsteady surface pressure coefficient shows larger values of the suction peaks and follows the trends of the measurements. The suction peak due to the strake vortex is underpredicted as in the steady-state solutions due to lack of grid resolution. The wing vortex strength and location are predicted reasonably well by the unsteady solution. The computed and measured surface pressure coefficient at a peak angle of incidence $\alpha = 29.2$ deg (phase angle $\phi = \pi$) are compared in Fig. 8c. At this angle of incidence the strake vortex is the strongest during the oscillatory cycle and suffers breakdown over the wing. The strake vortex interacts with the wing vortex, and at $x/c = 0.65$ the wing vortex is weaker compared to the strength obtained for lower angles during the oscillatory cycle. The computed unsteady surface pressure coefficient during the pitch-down motion at $\alpha = 22.4$ deg (phase angle $\phi = 3\pi/2$) is shown in Fig. 8d. The computed wing vortex suction peak is smaller than the steady flow suction peak, and the predicted surface pressure follows the trends of the experiment reasonably well.

The vortex structure and the location of strake and wing vortices are shown with the vorticity magnitude at several

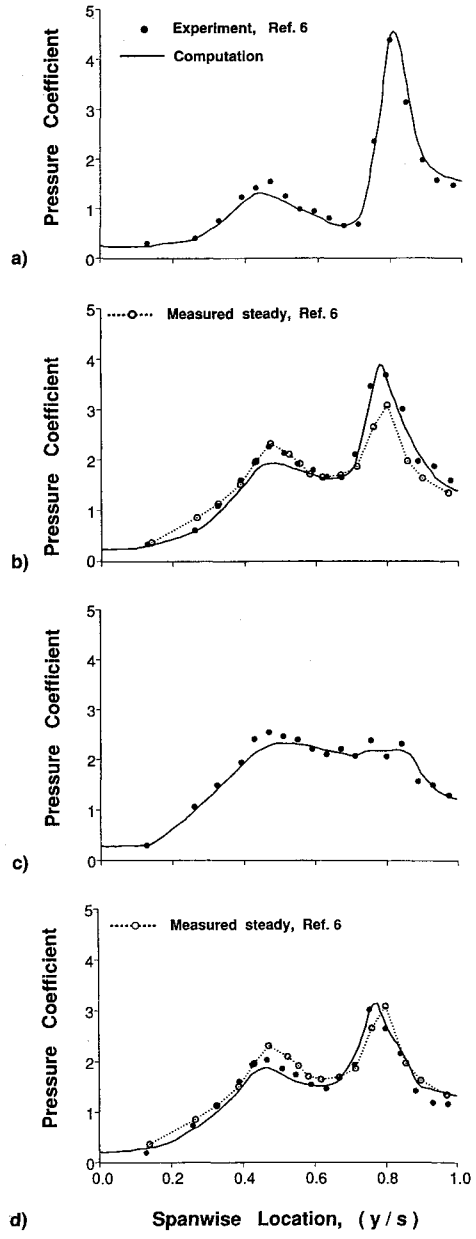

Fig. 8 Computed and measured surface pressure coefficient at a) α = 15.6 deg, ϕ = 0 and 2π; b) α = 22.4 deg, $\phi = \pi/2$; c) α = 29.2 deg, $\phi = \pi$; and d) α = 15.6 deg, $\phi = 3\pi/2$; M_∞ = 0.22, $\alpha(t)$ = [22.4 + 6.8 sin(ωt)] deg, k = 0.24, $Re_c = 4.0 \times 10^6$ (turbulent).

crossflow planes. The vortex trajectories are shown with particle traces released from the strake and wing leading edges. Instantaneous particle traces do not represent accurately unsteady flowfields. However, particle traces provide an approximate location of the vortex trajectory and breakdown location. The computed leeward-side flow structure at the minimum angle of attack is shown in Fig. 9a. At this angle of attack none of the vortices suffers vortex breakdown. During the pitch-up motion vortex breakdown develops first on the wing vortex. Figure 9b shows the computed leeward-side flow structure for the mean angle of incidence. During pitch-up lag of vortex breakdown was obtained and the vortex breakdown location was found further downstream compared to the fixed angle-of-attack case. At the maximum angle of incidence the strake vortex (Fig. 9c) also suffers vortex breakdown. At the mean angle of incidence during the pitch-down motion (Fig. 9d) the strake vortex over the wing is re-established and vortex breakdown is observed for the wing vortex only. The vortex breakdown location during pitch-down is

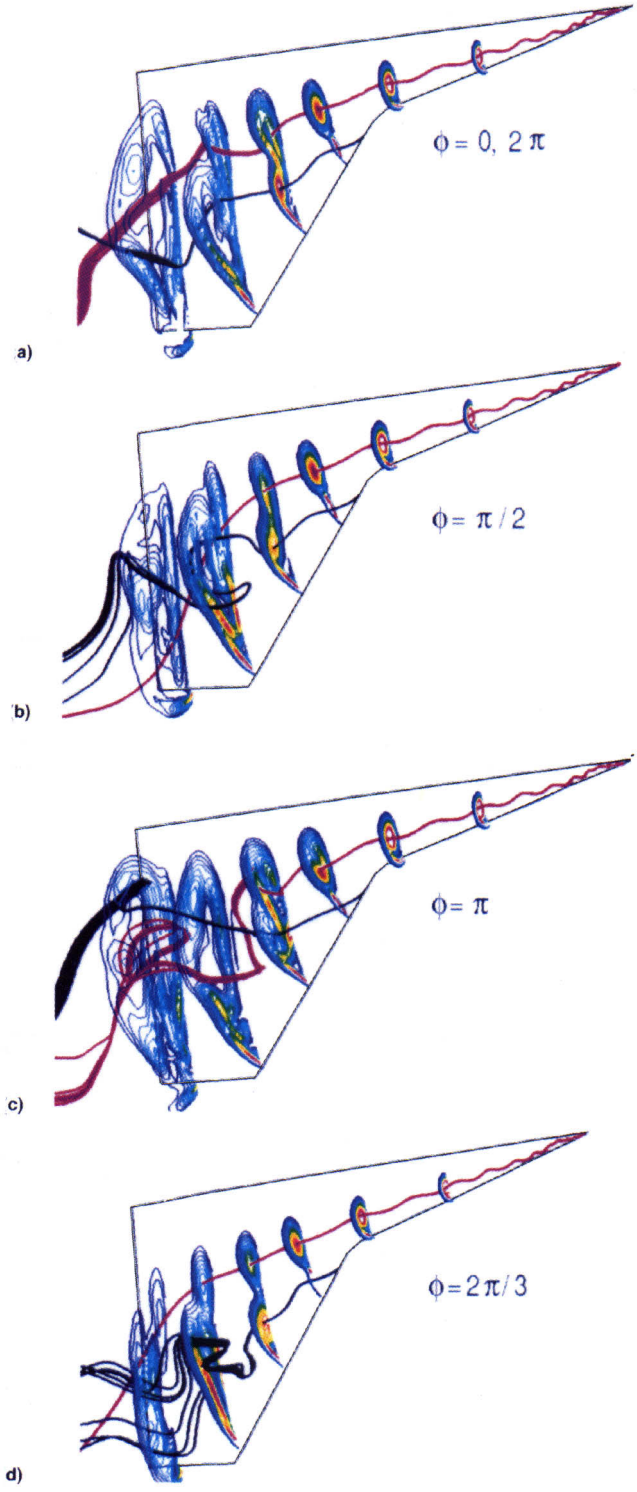

Fig. 9 Leeward-side flow structure shown by vorticity magnitude and particle traces at α = a) 15.6, b) 22.4, c) 29.2, and d) 15.6 deg; M_∞ = 0.22, $\alpha(t)$ = [22.4 + 6.8 sin(ωt)] deg, k = 0.24, $Re_c = 4.0 \times 10^6$ (turbulent).

found further upstream compared to the location obtained by the steady-state solution at the same fixed angle of incidence.

The structure of the leeward-side unsteady flowfield is further shown with particles that are released continuously from several fixed locations at the strake and wing leading edges. These particles are convected with the local computed velocity. The particle convection through the oscillatory cycle is computed with the UFAT code[21] using as input the computed, unsteady flowfields. The trajectories of the convected parti-

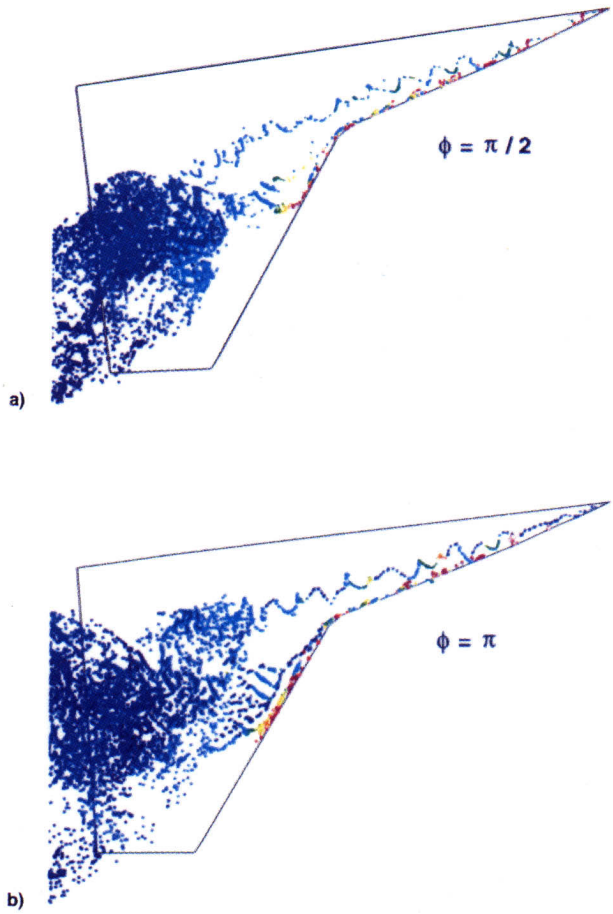

Fig. 10 Leeward-side flow structure shown with convected particles during the oscillatory cycle at α = a) 22.4-deg *up* and b) 29.2 deg; $M_\infty = 0.22$, $\alpha(t) = [22.4 + 6.8 \sin(\omega t)]$ deg, $k = 0.24$, $Re_c = 4.0 \times 10^6$ (turbulent).

cles resemble flow realizations obtained from a smoke flow visualization experiment. Snapshots from an animation of the convected particles at the mean angle during pitch-up and for the maximum angle $\alpha = 29.2$ deg are shown in Figs. 10a and 10b. Comparison of Figs. 10a and 10b with Figs. 9b and 9c, respectively, shows that convected particles provide a different realization of the unsteady flowfield.

Conclusions

An upwind-biased implicit scheme was utilized to investigate steady and unsteady vortical flows at high angles of attack over a double-delta wing configuration. Steady-state solutions for fixed angles of attack and unsteady solutions for a sinusoidal oscillatory motion were obtained. The steady-state solutions on the baseline grid were in agreement with the experiment, and grid refinement improved the predictions. The higher-order accuracy of the present scheme yielded equivalent solutions on smaller grid densities compared to solutions obtained with a second-order accurate method on denser grids. As the angle of attack increases, the grid resolution requirements for adequate resolution of the leeward-side vortical flowfield become very severe. Local grid refinement or a grid adaption scheme must be used for more accurate predictions of the higher angle-of-attack flows. The unsteady solutions were in agreement with the measurements and showed qualitative correlation with the experimental trends. The lags in surface pressure and vortex breakdown development due to the unsteady motion have been captured by the unsteady solution.

References

[1]Payne, F. M., and Nelson, R. C., "An Experimental Investigation of Vortex Breakdown on Delta Wings," *Vortex Flow Aerodynamics*, 1985, pp. 135–161 (NASA CP-2416).

[2]Kjelgaard, O., and Sellers, W. L., "Detailed Flowfield Measurements over a 75° Swept Delta Wing for Code Validation," AGARD Symposium on Validation of CFD, Lisbon, Portugal, May 1988.

[3]Schrader, K. F., Reynolds, G. A., and Novak, C. J., "Effects of Mach Number and Reynolds Number on Leading-Edge Vortices at High Angle-of-Attack," AIAA Paper 88-0172, Jan. 1988.

[4]Magness, C., Robinson, O., and Rockwell, D., "Control of Leading-Edge Vortices on a Delta Wing," AIAA Paper 89-0999, March 1989.

[5]Roos, F. W., and Kegelman, J. T., "An Experimental Investigation of Sweep-Angle Influence on Delta Wing Flows," AIAA Paper 90-0383, Jan. 1990.

[6]Cunningham, A. M., and Den Boer, R. G., "Low-Speed Unsteady Aerodynamics of a Pitching Strake Wing at High Incidence-Part II: Harmonic Analysis," *Journal of Aircraft*, Vol. 27, No. 1, 1990, pp. 31–41.

[7]Fujii, K., and Schiff, L. B., "Numerical Simulation of Vortical Flows over Strake-Delta Wing," *AIAA Journal*, Vol. 27, No. 9, 1989, pp. 1153–1162.

[8]Thomas J. L., Taylor, S. L., and Anderson, W. K., "Navier-Stokes Computations of Vortical Flows over Low Aspect Ratio Wings," AIAA Paper 87-0207, Jan. 1987.

[9]Kandil, O. A., and Chuang, A. H., "Unsteady Vortex-Dominated Flows Around Maneuvering Wings over a Wide Range of Mach Numbers," AIAA Paper 88-0317, Jan. 1988.

[10]Hsu, C. H., and Liu, C. H., "Prediction of Vortical Flows on Wings Using Incompressible Navier-Stokes Equations," Third International Congress of Fluid Mechanics, Cairo, Egypt, Jan. 1990.

[11]Rai, M. M., and Chakravarthy, S. R., "An Implicit Form of the Osher Upwind Scheme," *AIAA Journal*, Vol. 24, No. 5, 1986, pp. 735–743.

[12]Chakravarthy, S. R., Szema, K.-Y., Coldberg, U. C., and Corski, J. J., "Application of a New Class of High Accuracy TVD Schemes to the Navier-Stokes Equations," AIAA Paper 85-0165, Jan. 1985.

[13]Rai, M. M., "Unsteady Three-Dimensional Navier-Stokes Simulations of Turbine Rotor-Stator Interaction," Part I—Methodology, Part II—Results, *Journal of Propulsion and Power*, Vol. 5, No. 3, 1989, pp. 307–319.

[14]Barth, T. J., "Analysis of Implicit Local Linearization Techniques for Upwind and TVD Algorithms," AIAA Paper 87-0595, Jan. 1987.

[15]Steger, J. L., and Warming, R. F., "Flux Vector Splitting of the Inviscid Gas Dynamic Equations with Applications to Finite-Difference Methods," *Journal of Computational Physics*, Vol. 40, No. 2, 1981, pp. 263–293.

[16]Baldwin, B. S., and Lomax, H., "Thin Layer Approximation and Algebraic Model for Separated Turbulent Flows," AIAA Paper 78-275, Jan. 1978.

[17]Degani, D., and Schiff, L. B., "Computation of Turbulent Supersonic Flows Around Pointed Bodies Having Crossflow Separation," *Journal of Computational Physics*, Vol. 66, No. 1, 1986, pp. 173–196.

[18]Ekaterinaris, J. A., Coutley, R. L., Schiff, L. B., and Platzer, M. F., "Numerical Investigation of the Flow over a Double-Delta Wing at High Incidence," AIAA Paper 91-0753, Jan. 1991.

[19]Ekaterinaris, J. A., and Schiff, L. B., "Vortical Flows over Delta Wings and Numerical Prediction of Vortex Breakdown," AIAA Paper 90-0102, Jan. 1990.

[20]Krist, S. L., Thomas, J. L., Sellers, W. L., and Kjelgaard, S. O., "An Embedded Grid Formulation Applied to a Delta Wing," AIAA Paper 90-0429, Jan. 1990.

[21]Lane, D. A., "UFAT—A Particle Tracer for Time-Dependent Flow Fields," *Proceedings of the IEEE Visualization '94*, Washington, DC, 1994.